



# Material extrusion 3D printing of polyether-ether-ketone scaffolds based on triply periodic minimal surface designs: A numerical and experimental investigation

Nasim Sabahi<sup>a</sup>, Ehsan Farajzadeh<sup>b</sup>, Iman Roohani<sup>c</sup>, Chun H. Wang<sup>a</sup>, Xiaopeng Li<sup>a,\*</sup>

<sup>a</sup> School of Mechanical and Manufacturing Engineering, The University of New South Wales (UNSW Sydney), Sydney, NSW, 2052, Australia

<sup>b</sup> School of Chemical Engineering, The University of New South Wales (UNSW Sydney), Sydney, NSW, 2052, Australia

<sup>c</sup> Tissue Engineering and Biomaterials Research Unit, School of Biomedical Engineering, The University of Sydney, Sydney, NSW, 2006, Australia

## ARTICLE INFO

### Keywords:

Material extrusion  
Polyetheretherketone  
Triply periodic minimal surfaces (TPMS)  
Gradient-density  
Scaffold

## ABSTRACT

Polyether-ether-ketone (PEEK) scaffolds have recently emerged as a promising alternative to traditional metallic orthopedic implants. However, reproducing the intricate microstructure of natural bone in PEEK scaffolds, while simultaneously matching their mechanical properties presents a significant challenge. This challenge is particularly pronounced in clinical settings where prioritizing safety, efficiency, and cost-effectiveness demands innovative manufacturing approaches. In this study, and for the first time we designed, and 3D printed density-graded triply periodic minimal surfaces (TPMS) PEEK scaffolds achieved through cost-effective material extrusion 3D printing. Notably the scaffolds integrate Gyroid, Diamond and Schwartz P unit cells. The structures feature a relative density transition from 22 % to 68 %, achieving graded porosity with a diverse pore size distribution that mirrors natural bone microstructure. Our experimental and numerical investigation examined the impact of unit cell and density variations on manufacturability, morphological and mechanical characteristics of PEEK scaffolds. Micro-CT imaging validated the reproducibility of all scaffolds, with minor deviations in pore morphology attributed to material shrinkage. Finite element analysis and compressive tests revealed horizontal stress concentration in all gradient structures, contrasting with lattice-dependent deformations in uniform structures. The gradient Gyroid scaffold exhibited superior mechanical properties, with an elastic modulus and strength of 200 MPa and 5.15 MPa, surpassing Diamond (178 MPa, 4.3 MPa) and Schwartz (147 MPa, 4.1 MPa). In summary, the Gyroid and Diamond configurations excel among gradient scaffolds, displaying mechanical properties like trabecular bone and facilitating optimal pore size for effective bone regeneration.

## 1. Introduction

Polyether-ether-ketone (PEEK), a semi-crystalline high-temperature thermoplastic polymer, has garnered increasing attention as a promising alternative to conventional orthopedic metal implants and load-bearing bone scaffolds [1,2]. PEEK has excellent biocompatibility, in vivo stability, modulus of elasticity comparable to bone, high yield strength, and fatigue resistance, all of which make it a multipurpose biomaterial significantly convenient for bone tissue engineering applications [3–5]. In addition to material selection, the successful regeneration of bone requires precise design and fabrication of porous scaffolds capable of accurately replicating the intricate structure of natural bone required for tissue integration, thereby offering not only the required mechanical

properties to match the bone at the implantation site but also a supportive framework to allow the flow of oxygen, nutrients and efficient cell activity [6,7].

In contrast to traditional lattice structures, triply periodic minimal surfaces (TPMS) based scaffolds have been recently considered beneficial for bone regeneration. TPMS structures exhibit symmetry in three dimensions, which gives them advantageous topological, mechanical, and mass transport properties. Their unique combination of a high surface area-to-volume ratio and permeable pore architecture makes TPMSs a promising design for fabricating porous networks that closely resemble the surface curvature characteristics of human bone and could greatly facilitate efficient nutrient and oxygen transport, cellular migration, and extracellular matrix deposition [8–10].

\* Corresponding author.

E-mail address: [xiaopeng.li@unsw.edu.au](mailto:xiaopeng.li@unsw.edu.au) (X. Li).

<https://doi.org/10.1016/j.apmt.2024.102262>

Received 15 March 2024; Received in revised form 20 May 2024; Accepted 27 May 2024

Available online 3 June 2024

2352-9407/© 2024 The Author(s). Published by Elsevier Ltd. This is an open access article under the CC BY license (<http://creativecommons.org/licenses/by/4.0/>).

In recent years, additive manufacturing (AM) techniques have demonstrated significant potential in the fabrication of complex TPMS cellular structures. However, the majority of additively-manufactured TPMS constructs have relied on materials in powder form and laser-based methods, like selective laser melting and selective laser sintering [11–16]. For instance, Wang et al. [17] conducted a recent study wherein they designed and fabricated uniform TPMS PEEK scaffolds using the laser powder bed fusion (LPBF) technique. These scaffolds, based on Gyroid, Diamond, and I-WP unit cell designs, underwent a comprehensive investigation to assess the impact of unit cell type and volume fraction on manufacturing deviation and mechanical properties of LPBF-printed PEEK. Their findings revealed that the uniform Gyroid structure emerged as the optimal choice for both the design and LPBF fabrication of porous PEEK scaffolds, due to its superior manufacturing fidelity and relatively favorable mechanical properties. Furthermore, their findings confirm that the elastic moduli of PEEK TPMS scaffolds can match those of human trabecular bones. In another study by Chen et al. [18] they introduced a novel PEEK cage featuring lattice surfaces, fabricated through a high-temperature LPBF process. This lattice cage was specifically designed based on a uniform Diamond unit cell configuration, aiming to enhance mechanical responses, stress absorption, and deformation resistance, in contrast to conventional cages utilizing a trabecular structure. Their research revealed that the compression modulus and elastic limit of the lattice cage could be finely adjusted by manipulating the lattice-surfaced area, all while maintaining efficient energy absorption. Nonetheless, laser-based additive manufacturing approaches come with substantial cost and safety considerations. On the other hand, extrusion-based AM techniques, such as fused deposition modeling (FDM), offer a more cost-effective and safer alternative, especially in a hospital setting, where ensuring safety, efficiency, and cost-effectiveness are top priorities. FDM is a filament-based 3D printing technology that uses the melt extrusion method to selectively deposit thermoplastic filament layer-by-layer according to a CAD design [19,20].

Until recently, FDM printing of TPMS structures have primarily been restricted to low-temperature plastics. However, recent advances in FDM printing technology have paved the way for processing high-temperature medical-grade PEEK in the form of lattice structures. Over recent years, several studies have extensively examined the FDM printing of high-performance PEEK, highlighting various critical aspects. These include assessing the 3D printing stability of extruded PEEK, analyzing mechanical properties and the anisotropy of FDM-printed PEEK, investigating thermal conductivity, crystallization characteristics, and microstructures of both FDM-processed PEEK and PEEK composites. Overall, these studies collectively affirm the significant potential of FDM printing as a reliable method for processing PEEK material, demonstrating promising outcomes across diverse parameters [21].

Moreover, additional studies have focused on exploring FDM printing of conventional PEEK lattices featuring struts with flat or cylindrical surfaces [22–25]. These investigations consistently revealed favorable cell responses and mechanical properties of PEEK lattice structures that closely resemble those of human bone. However, there is very limited research investigating the viability of extrusion-based AM techniques to process PEEK materials for the production of TPMS cellular constructs. In a study conducted by Spece et al. [26], researchers explored the fabrication of porous PEEK structures through FDM printing. The designs of the porous structures were based on a simple rectilinear pattern and uniform Gyroid and uniform Diamond TPMS topologies. The pore structure morphology, mechanical properties, and in-vitro cytocompatibility of all FDM printed scaffolds were investigated. Their findings revealed open and interconnected porous networks aligned with the intended design, with TPMS structures exhibiting the highest level of mechanical strength. Notably, the study demonstrated that the porous PEEK samples exhibited enhanced cell attachment and activity compared to solid samples. In another study by the same research group

[27], they develop a predictive model aimed at establishing the correlation between the elastic modulus of uniform Gyroid and Diamond scaffolds and key parameters such as strut thickness, pore size, and porosity. In addition, their research explored how the build orientation during the FDM printing process influenced the failure mechanism and mechanical properties of the scaffolds. They reported that for both the uniform Gyroid and Diamond structures, the elastic modulus typically rose with enhanced strut thickness and decreased porosity. Interestingly, the modulus exhibited relative consistency along each porosity line.

While the current literature primarily focuses on the FDM printing of uniform TPMS PEEK scaffolds, it's imperative to acknowledge the inhomogeneous and non-uniform hierarchical structure found in natural bone tissue. Natural bone exhibits graded porosity with varied pore size distribution, and diverse property profiles [28]. Studies have shown the dual advantages of gradient porous structures for tissue-engineered scaffolds. Firstly, they closely mimic the complex anatomy of natural human bones better than uniform structures. Secondly, by allowing for variable structural parameters, they enable the balancing of both biological and mechanical properties of the scaffold. Therefore, the development of graded porous scaffolds is expected to facilitate the establishment of a functional environment conducive to enhanced cellular activity and reproduction [29–31]. Liu et al. [11] discovered that the TPMS method effectively generates gradients in multiple patterns, akin to natural tissue, in terms of both continuous topology and interconnectivity. Additionally, Han et al. [32] used SLM method and developed continuous functionally graded TPMS porous scaffolds based on the Schwartz Diamond architecture. They highlighted that a wide range of graded changes could optimize scaffold properties and pore space for bone tissue regeneration.

In this study, for the first time we designed and 3D printed density-graded TPMS PEEK scaffolds achieved through cost-effective FDM printing technology. Notably, these scaffolds integrate Gyroid, Diamond, and Schwartz P unit cells and the graded structures feature a continuous linear variation in wall thickness, ensuring a smooth density transition while maintaining porosity level. The manufacturability and accuracy of FDM printed graded TPMS scaffolds are investigated, with the focus on the main limitation associated FDM printing of complex designs and curved contours within these structures. Morphological properties of the scaffolds are characterized through optical microscopy, and micro-CT imaging. Both mechanical testing experiments and numerical investigations are conducted to investigate the impact of unit cell types and gradient structures on the mechanical properties, deformation mechanisms, and stress distribution of all FDM printed TPMS PEEK scaffolds. To better evaluate the impact of gradient structures on scaffold performance, we also design and fabricate uniform structures sharing the same average porosities and unit cell type, comparing their morphological properties, printability, and mechanical properties against the graded structures.

This study not only enhances our understanding of the spectrum of intricate structural and mechanical properties achievable through FDM printed PEEK TPMS scaffolds but also contributes to advancements in the field of bone tissue engineering by introducing fast, safe, and cost-effective approaches for the manufacturing of porous and customizable bone scaffolds resembling the intricate structure of natural bone.

## 2. Experimental details

### 2.1. Scaffold design and fabrication

TPMSs are complex 3D periodic surfaces that minimize surface area within a specified boundary. These surfaces divide the space into multiple interlocked regions, where each region forms a single, interconnected, and infinite component without enclosed empty spaces. Structures based on TPMS can be formed by the thickening of the minimal surface to generate sheet-based cellular constructs or by consolidating the volumes enclosed by the minimal surfaces to produce

skeletal-based cellular structures [12,33]. In this study, we focus on TPMS sheet scaffolds due to their exceptional mechanical properties and notably large surface area. To approximate TPMS structures, an implicit method is commonly employed, which represents surfaces through nodal equations and identifies zero-valued surfaces [34]. The nodal approximations for Schwarz P, Gyroid, and Diamond surfaces with cubic symmetries are described as follows in following Equations.

1. Schwarz P implicit surface:

$$\cos\left(\frac{2\pi}{a}\cdot x\right) + \cos\left(\frac{2\pi}{b}\cdot y\right) + \cos\left(\frac{2\pi}{c}\cdot z\right) = C \quad (1)$$

2. Diamond implicit surface:

$$\begin{aligned} &\cos\left(\frac{2\pi}{a}\cdot x\right) \cdot \cos\left(\frac{2\pi}{b}\cdot y\right) \cdot \cos\left(\frac{2\pi}{c}\cdot z\right) \\ &- \sin\left(\frac{2\pi}{a}\cdot x\right) \cdot \sin\left(\frac{2\pi}{b}\cdot y\right) \cdot \sin\left(\frac{2\pi}{c}\cdot z\right) \\ &= C \end{aligned} \quad (2)$$

3. Gyroid implicit surface:

$$\begin{aligned} &\sin\left(\frac{2\pi}{a}\cdot x\right) \cdot \cos\left(\frac{2\pi}{b}\cdot y\right) + \sin\left(\frac{2\pi}{c}\cdot z\right) \cdot \cos\left(\frac{2\pi}{a}\cdot x\right) \\ &+ \sin\left(\frac{2\pi}{b}\cdot y\right) \cdot \cos\left(\frac{2\pi}{c}\cdot z\right) \\ &= C \end{aligned} \quad (3)$$

where parameters  $a$ ,  $b$ , and  $c$  are the unit cell size in the directions X, Y, and Z, and  $C$  is the strut level parameter that regulates a unit's volume fractions (porosity). Consistently, a uniform unit cell size of  $a, b, c = 6.25$  mm was applied to all scaffolds, replicated four times in each direction, resulting in overall dimensions of  $25 \times 25 \times 25$  mm<sup>3</sup> for the designed structures. For the uniform structures, the strut thickness of Gyroid, Diamond, and Schwarz scaffolds were set at 1600  $\mu$ m, 1400  $\mu$ m, and 800  $\mu$ m, respectively. This deliberate adjustment was made with the specific goal of achieving a total porosity of 55 % (relative density of 45 %). Achieving an average porosity exceeding 50 % throughout the entire scaffold is crucial for fostering optimal bone ingrowth and promoting effective osseointegration [36]. For the graded TPMS structures, we introduced a linear and continuous variation in the wall thickness. Specifically, for the Gyroid structure the strut thickness was designed to linearly vary from 1070  $\mu$ m to 2120  $\mu$ m along the z direction. Similarly, for the Diamond and Schwarz scaffolds, the strut thicknesses were designed to vary from 1030  $\mu$ m to 1900  $\mu$ m and 600  $\mu$ m to 1200  $\mu$ m, respectively. As illustrated in Fig. 1, this meticulous variation was carefully designed to ensure that the relative density of all graded structures remained within the desired range of 22 % to 68 %. Consequently, this design approach results in the same average porosity as uniform scaffolds across all graded structures.

To calculate the relative density ( $\rho^*$ ) and porosity ( $P$ ) of the graded TPMSs, Eqs. (4) and 5 were employed [36]. These equations involve calculating the TPMS volume by multiplying its surface area ( $S_{TPMS}$ ) by the thickness ( $t$ ) and dividing it by the volume of a bulk structure with same dimensions, characterized by  $a, b$ , and  $c$ .

$$\rho^* = V_{scaffold} / V_{bulk} = S_{TPMS} \cdot t / (a \cdot b \cdot c) \quad (4)$$

$$P = 1 - \rho^* \quad (5)$$

A linear gradient in relative density and porosity ( $P$ ) on the Z axis are given by:

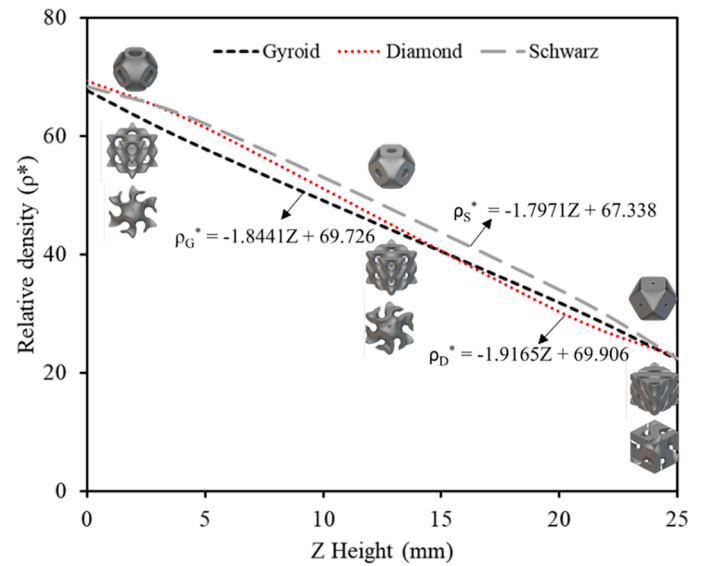


Fig. 1. Linear relationship between the relative density and the height of the TPMS structures.

$$\rho^* = k \cdot z + \rho_0^* \quad (6)$$

Where  $k$  and  $\rho_0^*$  can be calculated by the two points  $\rho_{z_{min}}^* = 68\%$  and  $\rho_{z_{max}}^* = 22\%$  or by finding the best-fitting line that maximizes precision when considering all the data points.

To determine the actual porosity of both uniform and graded scaffolds, dry weight measurements in air were employed and the porosity percentage of the scaffolds was calculated as follows [37]:

$$P = (1 - M_{scaffold} / M_{bulk}) * 100 \quad (7)$$

Where  $M_{scaffold}$  is the mass of scaffold in air and  $M_{bulk}$  is the theoretical mass of solid cubic sample with same dimensions. Measurements were repeated three times on three different samples.

Fig. 2 illustrates the unit cell of each TPMS structure and the final design, incorporating both uniform and graded structures consisting of four repeating unit cells with dimensions of  $a, b$ , and  $c$ .

Once the TPMS surface was generated using nTopology software, it was converted into a mesh representation that is compatible with 3D printing. The resulting mesh was then exported as an STL file. To further prepare the models for printing, the STL files were imported into Simplify 3D slicing software to generate the necessary G-code instructions for printing. The printing process utilized a high-temperature FDM printer (Apium P220, Karlsruhe, Germany) and PEEK filament (Apium PEEK 450). To ensure high-quality prints, specific printing parameters such as nozzle temperature, bed temperature, printing speed, extrusion multiplier, extrusion width, and cooling fan speed were selected based on manufacturer recommendations [38]. Additionally, all geometries were printed with 100 % infill density to create solid internal structures. The optimization conditions for nozzle diameter and layer height are detailed in the supporting document. Table 1 presents an overview of the FDM printing parameters that were used during the fabrication of the scaffolds.

## 2.2. Porous scaffold morphology

To evaluate the structural features and defects in all 3D printed scaffolds, we employed micro-CT characterization (Scanco Medical AG, Brüttisellen, Switzerland). The micro-CT procedure was conducted at a tube voltage of 160 kV, a tube current of 315  $\mu$ A, and a voxel resolution of 15.8  $\mu$ m. Subsequently, the acquired micro-CT images were processed and analyzed using the Avizo® software. The image data underwent

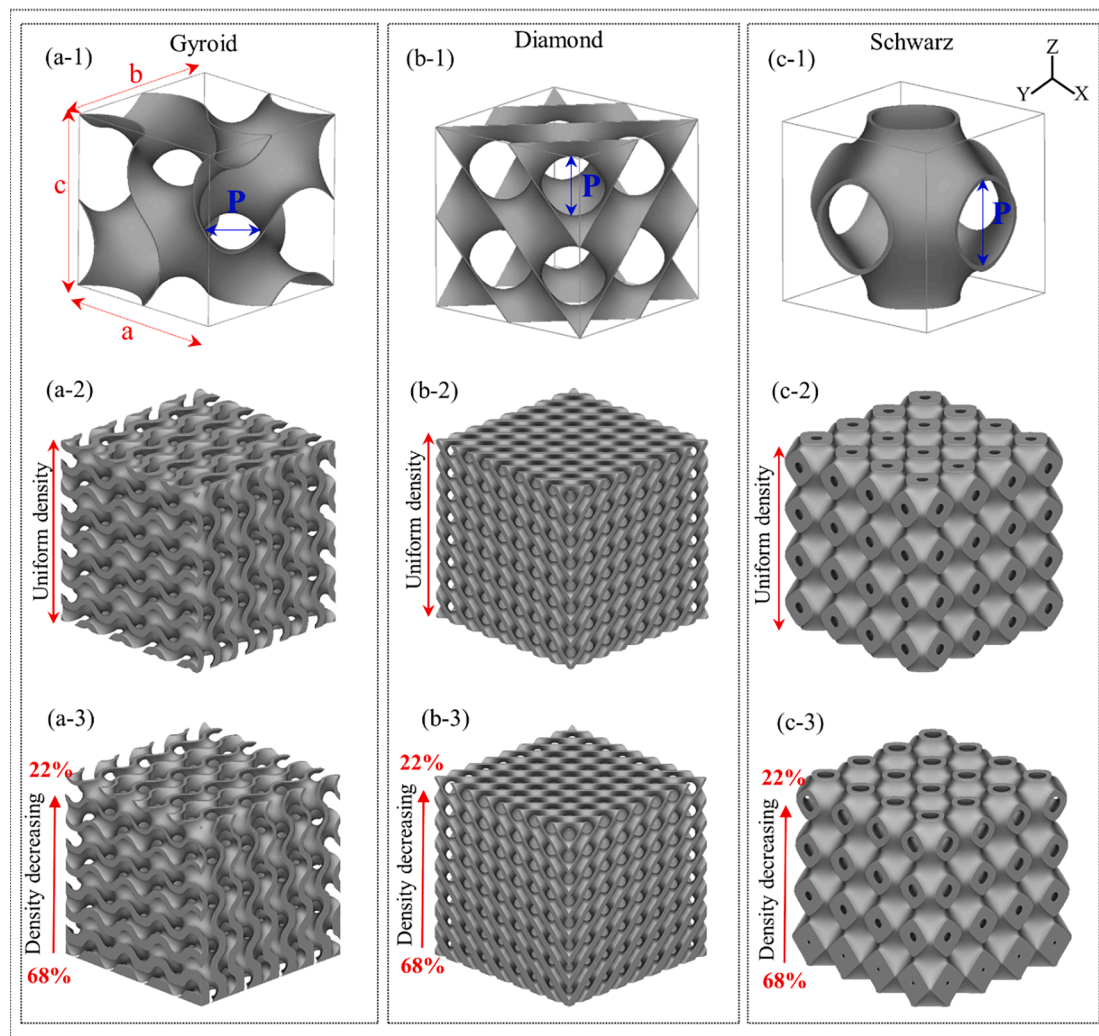


Fig. 2. CAD models of designed TPMS structures: (a-1) Gyroid unit cell, (a-2) uniform Gyroid, (a-3) graded Gyroid, (b-1) Diamond unit cell, (b-2) uniform Diamond, (b-3) graded Diamond, (c-1) Schwarz P unit cell, (c-2) uniform Schwarz P, (c-3) graded Schwarz P. The scaffold has a total height of 25 mm, with a relative density of 68 % assigned at a Z height of 25 mm, and a relative density of 22 % assigned at a Z height of 0 mm.

**Table 1**  
Printing parameters for printing the TPMS structures.

Parameter	Value
Nozzle diameter	0.2 mm
Primary layer height	0.08 mm
Infill extrusion width	100 %
Extruder temperature	480 °C
Print bed temperature	130 °C
Print speed	2000 mm/min
Extrusion multiplier	0.9
Cooling	60 %

preprocessing, involving the removal of noise and artifacts from the scans and adjusting the image resolution as needed. Following this, we generated volume renderings to create a 3D representation of the internal structure, and fine-tuned parameters such as the transfer function, opacity, and color maps. Finally, the morphologies of the scaffolds were exported for further analysis. In addition, digital optical microscopy (Olympus SDX510) was used to assess and record the surface quality and the presence of microdefects in the printed structures.

### 2.3. Static compression testing

#### 2.3.1. Experimental compression testing

The mechanical properties of the 3D printed scaffolds were evaluated by compression test using a universal testing system (Instron testing machine 3369 model) equipped with a 50 kN load cell. In accordance with ASTM D695–15 standard [39], printed scaffolds ( $n = 3$  per group) were compressed based on an 80 % deformation at a constant crosshead speed of 1.3 mm/min at room temperature. The load was applied in a perpendicular manner to the direction of layer deposition. The obtained data were used to generate stress-strain curves for each porous design. From these curves, the modulus of elasticity and yield strength (determined as the 0.2 % offset stress) were calculated [40]. The video camera (BirdDog PF120 NDI) captured the deformation behavior of all the TPMS scaffolds.

#### 2.3.2. Numerical compression testing

In this study, ANSYS Workbench 2022R2 was used for Finite Element Analysis (FEA) of lattice structures' stress distribution and compression performance, following the ASTM D695–15 standard used in experimental compression tests. The computational domain employed for this numerical simulation included the top and bottom die, as well as the load direction. All lattice structure dimensions were  $25 \times 25 \times 25 \text{ mm}^3$ , and the plates were sized at  $35 \times 35 \times 2 \text{ mm}^3$ . A displacement of 12.5 mm,

equivalent to a 50 % strain, was applied to the lattice structures for simulation. For meshing, a non-linear mechanical mesh was created with 0.5 mm-sized elements, chosen to precisely capture significant deformations and alterations in the geometric configuration of the lattice structures. A mesh independence test was conducted to ensure accurate results, using approximately 1 million elements to maintain solution accuracy. In terms of boundary conditions, the top die was set as "bonded" to establish a rigid connection with the lattice structure. In contrast, the bottom die had a frictionless boundary condition to facilitate free sliding with the ground, reducing computational costs. Analysis type is static structural analysis, and the Newton-Raphson method was employed in "full" mode to precisely monitor deformations and geometry alterations in the lattice structures. Regarding material properties, as the mechanical characteristics of PEEK were not present in the ANSYS Workbench material database, they were manually specified and integrated into the simulation. Young's modulus, Poisson's ratio, tensile yield strength, and compressive yield strength were set at 3.76 GPa, 0.3779, 70.3 MPa, and 87 MPa, respectively. Fig. 3 illustrates the computational domain featuring the gyroid uniform design used in the numerical simulation.

### 3. Results and discussions

#### 3.1. Sample morphology

In Fig. 4, we present the FDM-printed scaffolds along with micro-CT images, orthogonal plane cuts, and optical microscopy images captured from top views of the scaffolds.

The structural characteristics, including average pore size, strut size, and porosity for each design, are provided in Table 2, along with corresponding values obtained from the actual FDM-printed scaffolds.

Micro-CT scanning results revealed that the pores within the FDM printed constructs were open and interconnected. Importantly, all TPMS scaffolds printed using FDM closely matched the intended designs. There were no significant deviations observed in the average pore size, strut size, and porosity for each geometry when compared to their original designs. This highlights the effective optimization of FDM printing process parameters, ensuring high precision and accuracy in 3D printing the designed TPMS structures. Using Eq. (7) the actual porosity of all FDM printed scaffolds was determined. The variation between the designed and measured porosity was negligible. The uniform Gyroid, Diamond, and Schwarz scaffolds displayed actual porosities of 55 %, 54.9 %, and 55.2 %, respectively. In the case of graded structures, these values were 55.2 %, 55 %, and 55.1 %, respectively.

The size of the pores in the scaffold was determined by measuring the diameter of the largest sphere that can pass through the narrowest channel, as indicated in Fig. 2a-1, 2b-1, and 2c-1 [10]. The actual pore sizes of FDM-printed gradient Gyroid, Diamond, and Schwarz scaffolds fell within the ranges of 590–1340  $\mu\text{m}$ , 700–1430  $\mu\text{m}$ , and 218–1745

$\mu\text{m}$ , respectively. Fig. 5 presents a depiction of the measured pore sizes for all graded scaffolds in relation to their respective Z heights. Notably, graded Gyroid and Diamond structures exhibited comparable pore size ranges, while the graded Schwarz P scaffold showed a wider range of pore sizes. Additionally, it was observed that the printed scaffolds had pore sizes smaller than their designed sizes. In the case of uniform Gyroid, Diamond, and Schwarz scaffolds, the actual pore sizes were 1050  $\mu\text{m}$ , 1160  $\mu\text{m}$ , and 1350  $\mu\text{m}$ , respectively. The average differences between the designed and printed pore sizes were  $-20 \mu\text{m}$ ,  $-40 \mu\text{m}$ , and  $-30 \mu\text{m}$ , respectively. The negative values indicate pore shrinkage, which is a typical challenge encountered in FDM printing. During the hot extrusion process, heated polymer material is deposited from the nozzle, which then cool and solidify on previous layers. This cooling process leads to uneven heat distribution and temperature variations, resulting in internal stresses and shrinkage. This shrinkage can cause the printed pore to be slightly smaller than their intended design [41]. It is worth noting that the selection of materials and their thermal properties play a crucial role in determining the morphological accuracy of FDM printed porous structures. Materials with lower thermal expansion coefficients generally experience less shrinkage during printing, leading to improved morphological accuracy in the final parts. Hence, for printing complex porous structures, materials like PEEK, known for their exceptionally low thermal expansion coefficient compared to other engineering polymers, are a favorable choice [42,43].

Previous studies have disclosed the use of scaffolds with mean pore sizes ranging from 100  $\mu\text{m}$  to 1500  $\mu\text{m}$  in bone tissue engineering applications, demonstrating successful bone growth and tissue vascularisation [35,44,45]. Table 2 and Fig. 5 highlight that the attained pore sizes in all uniform scaffolds, graded Gyroid, and graded Diamond scaffolds align with the recommended range for optimal bone regeneration. Notably, the graded Schwarz P scaffold yielded larger pore sizes, specifically 1745  $\mu\text{m}$  at a Z height of 3.125 mm. Previous studies have also noted that when scaffolds with the same volume fraction are compared, the Schwarz P design tends to exhibit larger pore sizes in comparison to the Gyroid and Diamond scaffolds. This finding suggests that the specific geometric arrangement of the Schwarz P structure allows for relatively larger void spaces within the material [39].

#### 3.2. Deformation behavior

Finite element (FE) simulation was employed to analyze the distribution of stress within six TPMS scaffolds when subjected to a strain of 50 %. Fig. 6 illustrates the stress distributions at various strains for all scaffolds. The FE analysis revealed that the stress distribution and deformation behavior is influenced by the scaffold architecture, highlighting the importance of scaffold design in determining stress distribution. Notably, distinct variations in stress patterns were observed between the graded and uniform structures. In the graded structures, the highest stress concentration was consistently observed at the top surface, as shown in Fig. 6a-1, 6b-1, and 6c-1 at a strain of 30 % and 40 % for the Gyroid, Diamond, and Schwarz P graded structures. This observation can be attributed to the limited thickness of the graded scaffolds, leading to a concentration of load-bearing forces in this region. In contrast, the stress distribution in the uniform structures displayed lattice-dependent variations. For the uniform Gyroid and Diamond scaffolds, the highest stress values were found in the diagonal direction which may result in the appearance of slippage along this direction, as depicted in Fig. 6a-2 and 6b-2 at a strain of 50 % for the Gyroid uniform and Diamond uniform structures. Previous studies have reported similar observations regarding stress distribution in uniform Gyroid and Diamond structures [17,46]. This pattern suggests that the diagonal paths within the lattice structure bear the maximum load and experience the highest stress levels [17]. Conversely, in the uniform Schwarz P scaffold, the stress distribution was highest in the horizontal direction at the top of each unit cell, as illustrated in Fig. 6c-2 at a strain of 50 % for the Schwarz P uniform structure. This finding indicates a preference for load

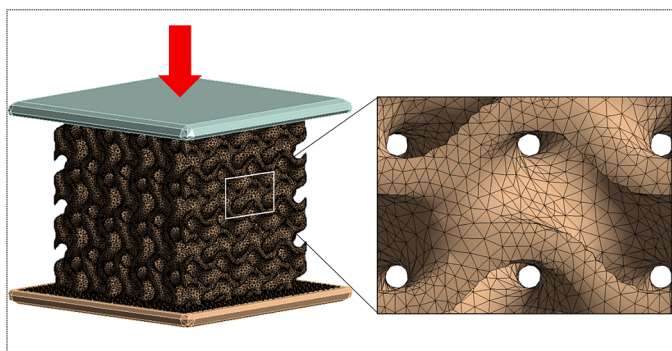
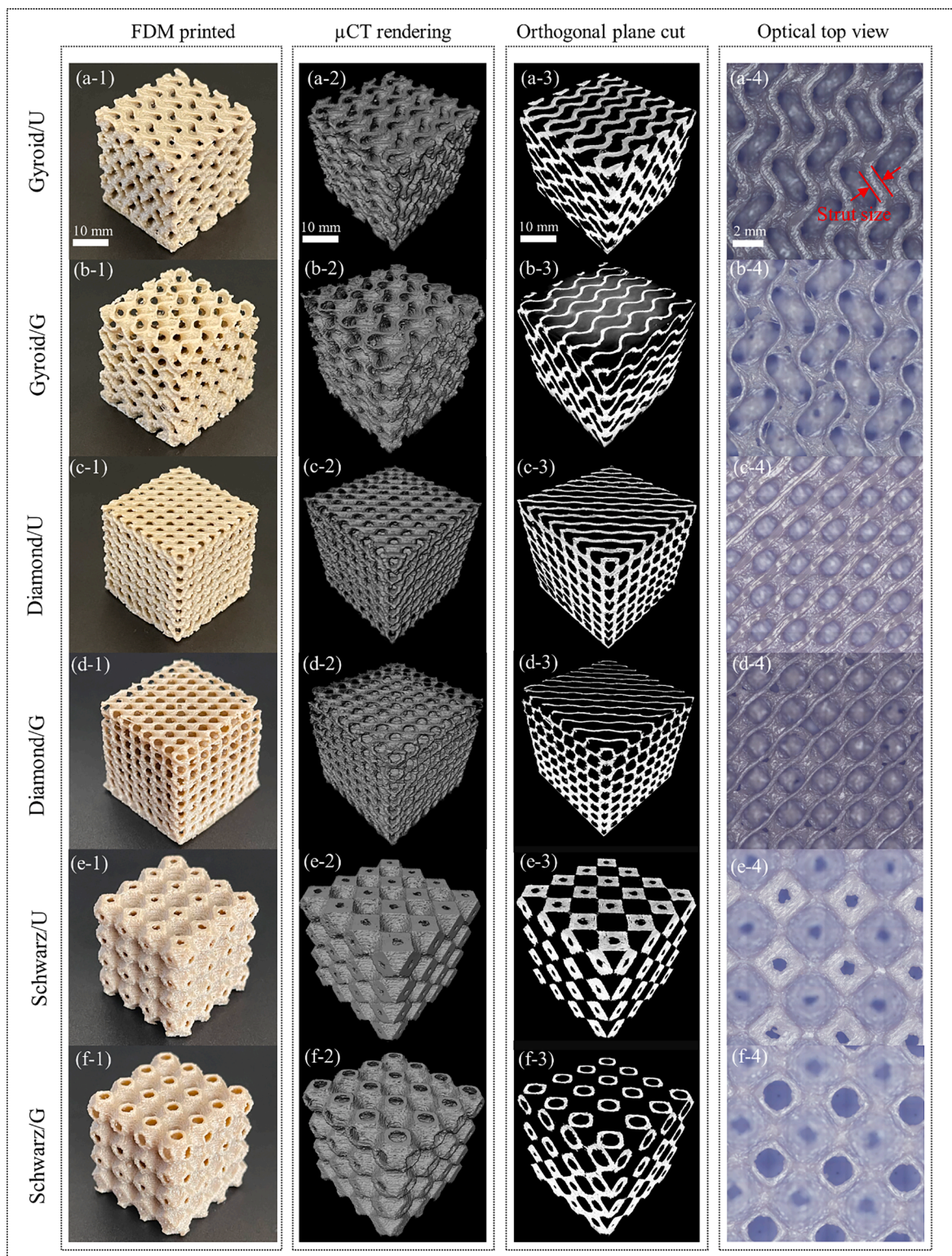


Fig. 3. Computational domain featuring the Gyroid uniform design used in the numerical simulation.



**Fig. 4.** (First column) FDM printed, (Second column) 3D  $\mu$ CT rendering images, (Third column) Orthogonal plane cut, and (Fourth column) top view of optical microscopy images for (a) Gyroid uniform, (b) Gyroid graded, (c) Diamond uniform, (d) Diamond graded, (e) Schwarz P uniform, and (f) Schwarz P graded TPMS structures.

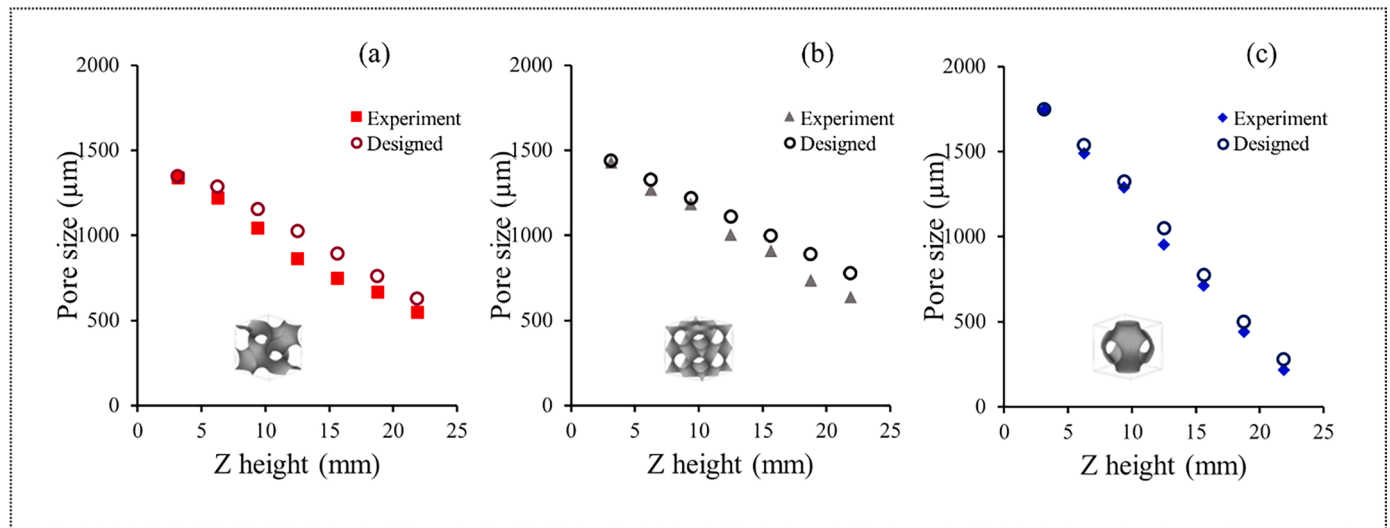
transfer along the horizontal plane of the Schwarz P lattice, resulting in localized stress accumulation in this direction.

Fig. 7 shows the deformation and collapse behaviours of all FDM-printed PEEK TPMS scaffolds with same porosity. As the upper die moved down, all scaffolds displayed elastic-plastic deformation prior to reaching the point of fracture occurred. In terms of the fracture behavior

of the graded TPMS scaffolds, similarities were observed during the compression tests for the three different TPMS structures. For all graded scaffolds, fracture initiation consistently occurred at the top surface, which have the thinnest thickness. Cracks initiated at the thinnest layers and then progressively extended to the thicker region in a sequential layer-by-layer fashion. This phenomenon can be attributed to the

**Table 2**  
The detailed information of both designed and FDM printed scaffolds.

		Gyroid		Diamond		Schwarz P	
		Uniform	Graded	Uniform	Graded	Uniform	Graded
CAD Design	Pore size ( $\mu\text{m}$ )	1070	630–1350	1200	780–1440	1380	280–1750
	Average Porosity (%)	55	55	55	55	55	55
	Strut ( $\mu\text{m}$ )	1600	1070–2120	1400	1030–1900	800	600–1200
FDM printed (Average)	Pore size ( $\mu\text{m}$ )	1050	590–1340	1160	700–1430	1350	218–1745
	Average Porosity (%)	55	55.2	54.9	55	55.2	55.1
	Strut ( $\mu\text{m}$ )	1620	1120–2120	1430	1070–1910	820	630–1250



**Fig. 5.** Pore sizes of the graded (a) Gyroid, (b) Diamond, (c) Schwarz scaffolds against the Z height.

gradual enhancement of structural strength resulting from the incremental increase in wall thickness. However, it is important to note that in the case of graded Schwartz scaffold, early indications of cracks in the lower layers were observed at a strain of 10 % and 20 %, particularly near the pore curves. This observation is supported by FEA analysis results (Fig. 6) which indicates a higher stress distribution at the top surface gradually decreasing in the Z direction as the structure's thickness increases in the graded structures. In the uniform Gyroid structure, cracks were initially observed in the diagonal direction at around 30 % strain. However, these cracks disappeared as the strain increased to approximately 40 %. The efficient interlocking and direct contact between neighbouring cellular structures facilitated rapid crack filling and the elimination of shear bands within the uniform structure. FE analysis in Fig. 7d further supported this finding, highlighting the likelihood of higher tension in the diagonal direction. Additionally, Fig. 6a-2 revealed a susceptible and fragile stress distribution along the diagonal direction in the uniform Gyroid structure.

Similar to the Gyroid scaffolds, detailed observations of the Diamond uniform structure revealed crack initiation at the center of the structure at a strain of 30 %. These cracks then gradually propagated along the diagonal direction. The collapsing process began at the bottom surface, resulting in layer-by-layer collapses. The fracture behavior of Gyroid and Diamond scaffolds was further supported by Fig. 7d and e, illustrating higher stress concentration along the diagonal direction, further validating the experimental observations. Fig. 7f also highlights the presence of stress concentration regions near the pore curves in the Schwarz P scaffolds. These regions are particularly susceptible to failure initiation and eventual fracture. The existence of hollow curves within the Schwarz P structure introduces inherent vulnerabilities in terms of stress distribution and load-bearing capacity. The concentrated stresses within these hollow curves increase their susceptibility to fracture and failure. These findings align with previous studies in the literature,

which have consistently shown through simulation analyses the influence of hollow layers on the deformation behavior and structural integrity of lattice and honeycomb structures [47].

### 3.3. Mechanical properties

One of the key requirements for bone scaffolds is to possess mechanical properties that is similar to natural bone, enabling them to withstand the stresses encountered during tissue regeneration. This requirement is essential for ensuring the scaffolds' ability to provide structural support and stability throughout the healing process. The mechanical properties of TPMS scaffolds are greatly influenced by factors such as density and the type of unit cell employed. These parameters play a significant role in determining the strength, stiffness, and overall mechanical behavior of the scaffolds. By optimizing these parameters, the mechanical performance of bone scaffolds can be tailored to provide the necessary support and functionality for successful tissue regeneration. Fig. 8 shows the numerical and experimental compressive stress-strain curves of our FDM printed uniform and graded TPMS scaffolds with different unit cell design. Fig. 8a-1, b-1, and 8c-1 provide a comprehensive view of the mechanical behavior of the Gyroid, Diamond, and Schwarz P scaffolds under compression, illustrating their response up to a strain of 80 %. All structures exhibit a typical mechanical response during compression, characterized by initial linear elasticity, followed by a long plateau stress stage and final densification. As densification begins, the stress increases rapidly, and the structures behave like solid materials due to self-contacting surfaces. In the case of the uniform scaffolds, a linear elastic behavior is observed in the initial elastic region, spanning from 0 % to 10 % strain, where the stress is directly proportional to the applied strain. The elastic modulus (E) of each scaffold was calculated from this region. As shown in Fig. 8c-1, the uniform Schwarz P scaffold display a peak stress of about 18.1 MPa at

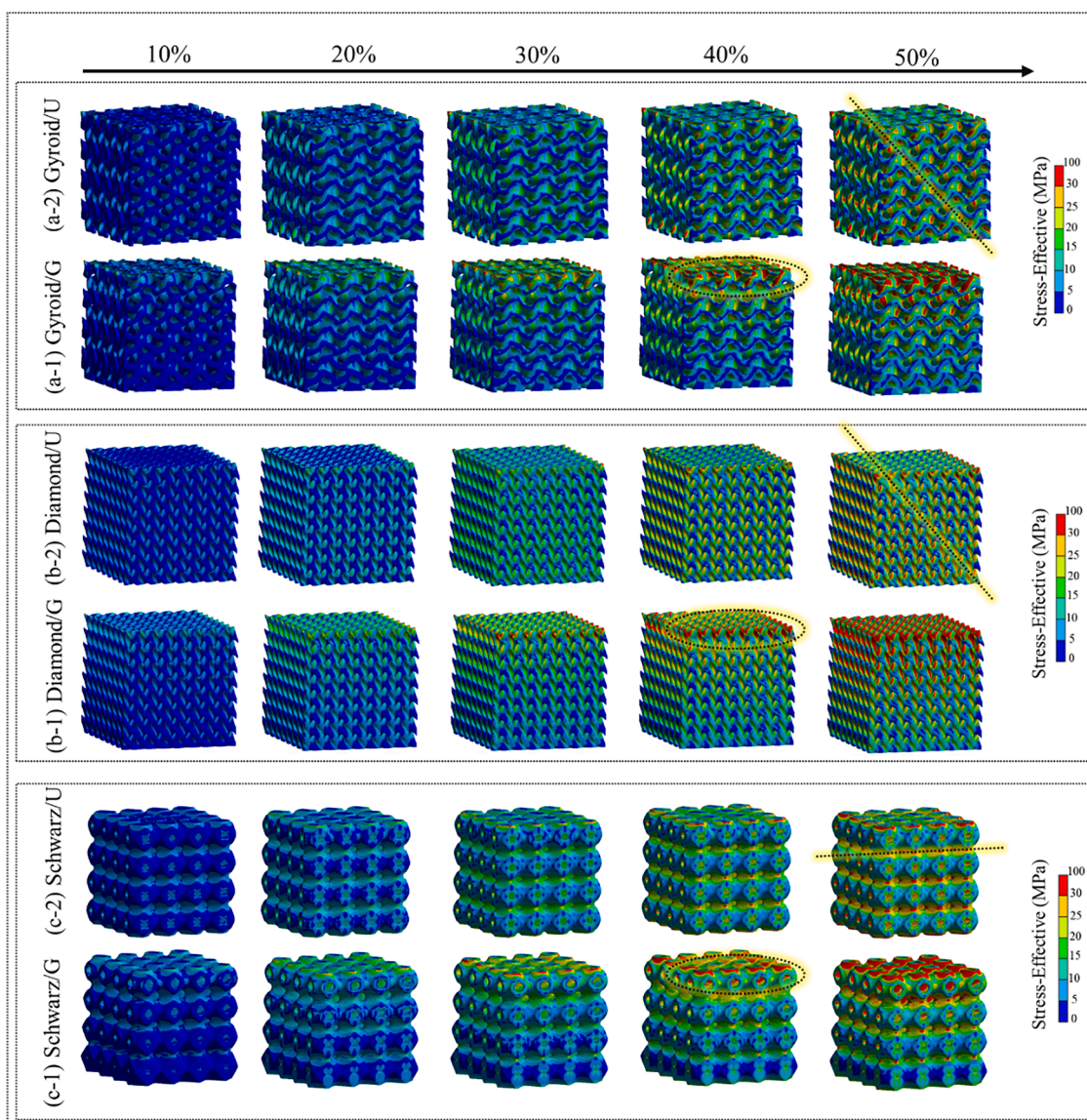


Fig. 6. Stress distribution of TPMS scaffolds under 10–50 % of strain for (a) Gyroid, (b) Diamond, and (c) Schwarz P with uniform and graded structures.

the end of the linear elastic phase. Subsequently, it demonstrates a softening behavior and stress fluctuations within the second region, identified as the plateau region. Notably, there are minor strength reductions observed in comparison to the peak stress. In contrast, uniform Gyroid and Diamond scaffolds lack a distinct peak stress, showing a continuous hardening behavior with minimal stress fluctuations in the plateau region (Fig. 8a-1, b-1). The second region, known as the plastic plateau, extends from approximately 15 % to 50 % strain. During this phase, the scaffolds undergo significant plastic deformation without a significant increase in stress. This indicates the scaffolds' ability to withstand high strains while maintaining a relatively constant stress level. The third region, referred to as the densification region, occurs beyond 50 % strain. In this region, the scaffolds experience a progressive increase in stress as the structure becomes more compact and denser due to compression [12,48].

The stress-strain curves of the graded scaffolds also exhibit the three distinct regions observed in the uniform scaffolds. However, in the case of the graded structures, visible fluctuations are observed in the plateau region of the compression tests for all scaffolds with Gyroid, Diamond, and Schwarz P unit cell designs. Fig. 8a-2 through 8c-2 illustrate a closer examination of specific regions of interest within the stress-strain

curves, allowing for a detailed exploration of the scaffolds' mechanical behavior. Moreover, Fig. 8a-3, b-3, and 8c-3 display the FE simulated stress-strain curves for the same scaffolds, demonstrating good agreement with the experimental results. For the graded Gyroid structure, a descent in the stress level is observed at around 20 % strain (Fig. 8a-1). This can be attributed to the occurrence of structural cracks, which were visually observed during the compression test at this stage. The presence of these cracks introduces local stress concentration and weakens the overall structural integrity, leading to the observed drop in stress. In the case of the Diamond and Schwarz P graded structures, even more pronounced fluctuations are observed in the stress-strain curves. These fluctuations can be attributed to the collapse of individual layers, primarily occurring at the top surfaces of the structures. As previously discussed, these top layers are typically the thinnest, making them more susceptible to deformation and collapse under compressive loading (Fig. 7). The collapse of these layers introduces variations in stress distribution along the structure, resulting in the observed fluctuations in the stress-strain curves. FE simulation results also exhibit fluctuations, although they may not precisely match the fluctuations observed in the experimental data. This disparity between the experimental and FE results may be attributed to the reduced thickness of the struts in the

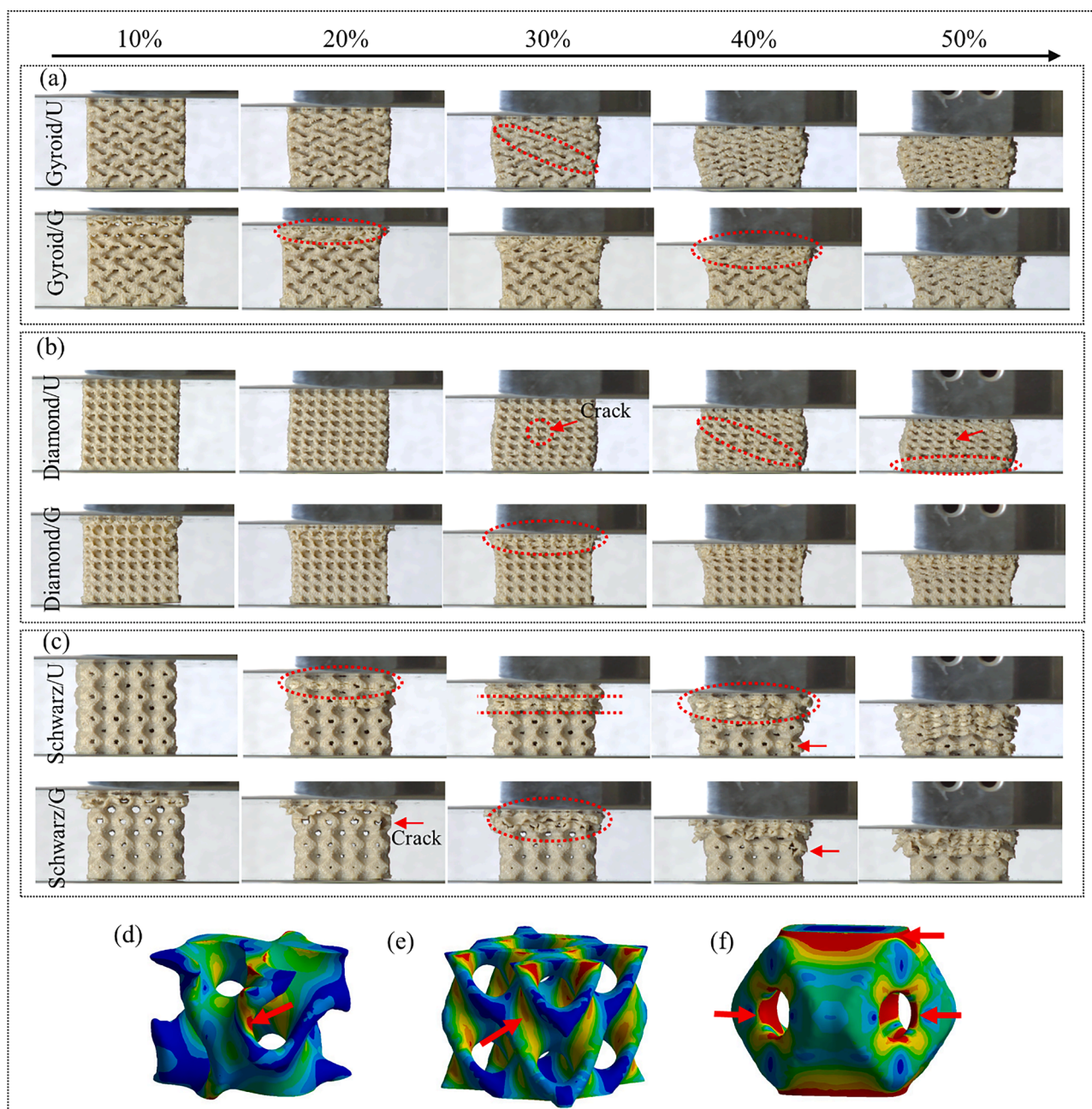


Fig. 7. Experimental deformation behavior of (a) Gyroid, (b) Diamond, and (c) Schwarz P structures under compressive load, and FE stress distribution of their unit cells: (d) Gyroid, (e) Diamond, and (f) Schwarz P. Stress concentration points are indicated by the red arrows.

numerical models, which can delay the contact of collapsed layers [49].

Fig. 9 and Table 3 present the compressive modulus and compressive yield strength of all TPMS scaffolds, comparing FE simulations and experimental results.

Focusing on the influence of unit cell type and structure design on the mechanical properties of PEEK TPMS scaffolds, we noted considerable variations in both elastic modulus and compressive strength values depending on the scaffold architecture for uniform scaffolds. The uniform Gyroid and uniform Diamond scaffolds exhibited an earlier onset of densification compared to the Schwarz P structure, indicating a higher level of elasticity. This suggests that these scaffolds possess greater resistance to compression, requiring more force to reach their maximum compressive strength. Specifically, the Gyroid, Diamond, and Schwarz P scaffolds demonstrated elastic moduli of 402 MPa, 343 MPa, and 234 MPa, respectively. Moreover, their respective compressive strengths

were measured at 24.7 MPa, 21.96 MPa, and 18.24 MPa. Previous studies have reported similar results, indicating the impact of unit cell type on the elastic modulus and compressive strength of additively manufactured TPMS structures [49,50]. The graded Gyroid scaffold exhibited the highest elastic modulus of 200 MPa and compressive strength of 5.15 MPa, while the Diamond and Schwarz graded scaffolds displayed lower values of 178 MPa and 147 MPa for elastic modulus, and 4.3 MPa and 4.1 MPa for compressive strength, respectively. Previous studies have provided a range of elastic modulus and compressive strength values for human trabecular bone, spanning from 10 to 3000 MPa and 0.1 to 45 MPa, respectively [51,52]. Notably, our findings demonstrated that the mechanical properties of our FDM printed PEEK scaffolds, including both uniform and graded structures utilizing various Gyroid, Diamond, and Schwarz P unit cell types, were comparable to the properties observed in trabecular bone (Fig. 9d). These results suggest

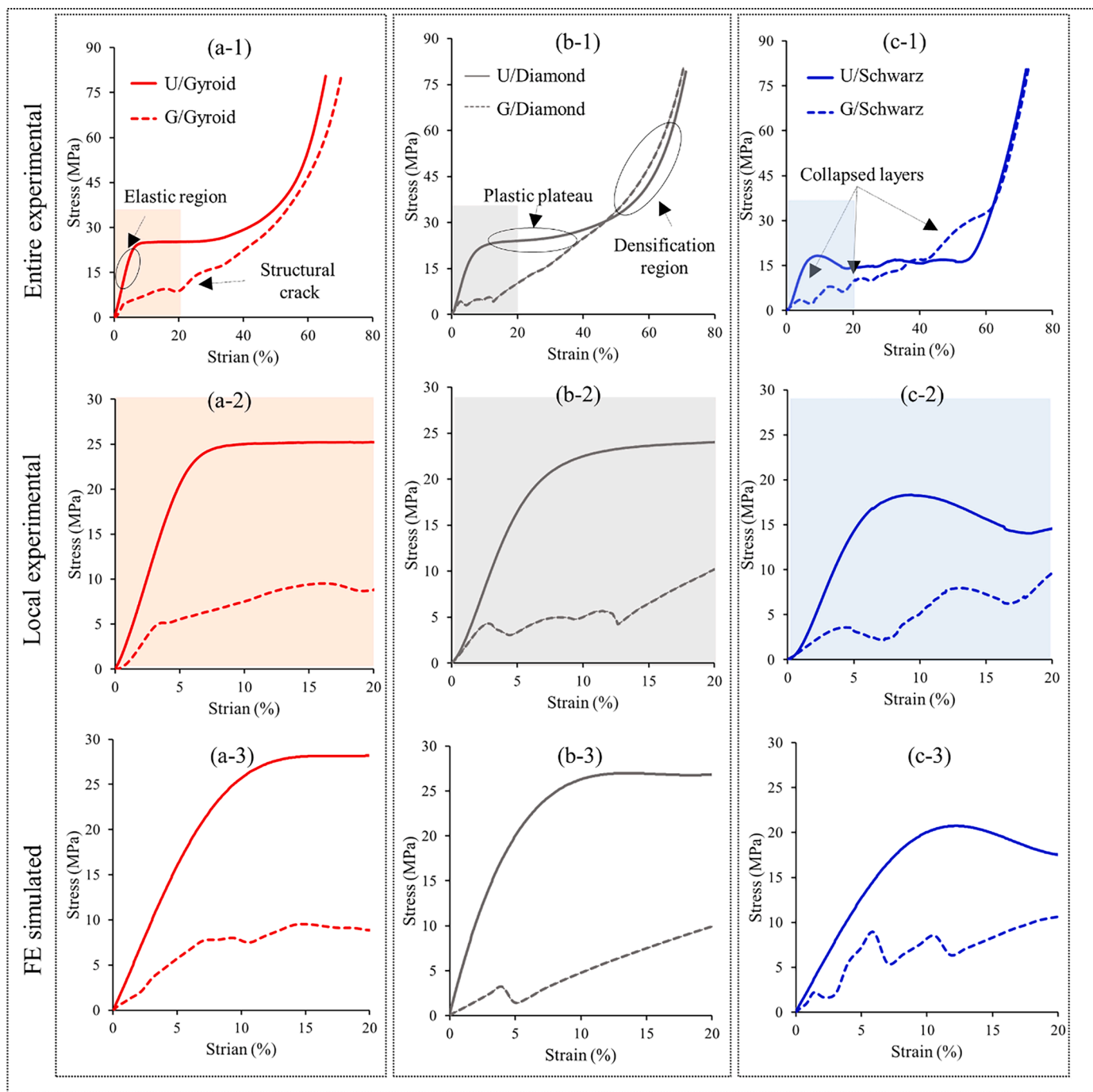


**Fig. 8.** Mechanical behavior of three PEEK TPMS scaffolds: entire experimental stress-strain curves for (a-1) Gyroid, (b-1) Diamond, and (c-1) Schwarz P, experimental stress-strain curves at local regions for (a-2) Gyroid, (b-2) Diamond, and (c-2) Schwarz P, stress-strain curves obtained from FE simulations for (a-3) Gyroid, (b-3) Diamond, and (c-3) Schwarz P scaffolds.

that our fabricated scaffolds have the potential to exhibit mechanical characteristics similar to native bone tissue, making them promising candidates for tissue engineering applications. Fig. 9d presents a comparison of the mechanical properties between our developed TPMS scaffolds and existing PEEK scaffolds fabricated using fused filament fabrication technology. Su et al. [23] investigated rectilinear PEEK samples and found compressive strength and modulus values of 23 MPa and 397 MPa, respectively. Feng et al. [24] tested FFF rectilinear lattice samples with approximately 60 % porosity and pore sizes ranging from 260 to 556  $\mu\text{m}$ . They reported ultimate compressive strength values between 31 and 60 MPa and elastic modulus values ranging from 231 to 368 MPa. In a recent study, Spec et al. [26] fabricated rectilinear,

uniform Gyroid, and uniform Diamond scaffolds using FDM printing. The TPMS-inspired structures, with a pore size of 600 and porosity of approximately 70 %, demonstrated higher mechanical strength compared to the traditional rectilinear scaffold. The uniform Diamond scaffold exhibited a strength of 17.1 MPa, the uniform Gyroid scaffold had a strength of 14.8 MPa, while the rectilinear scaffold had a lower strength of 6.6 MPa. While no specific studies on graded TPMS-inspired PEEK scaffolds were found for direct comparison, previous research has investigated porous PEEK structures created through FDM printing method. Remarkably, the mechanical properties observed in our study for TPMS scaffolds showed similarities to those reported in the literature for porous PEEK structures.

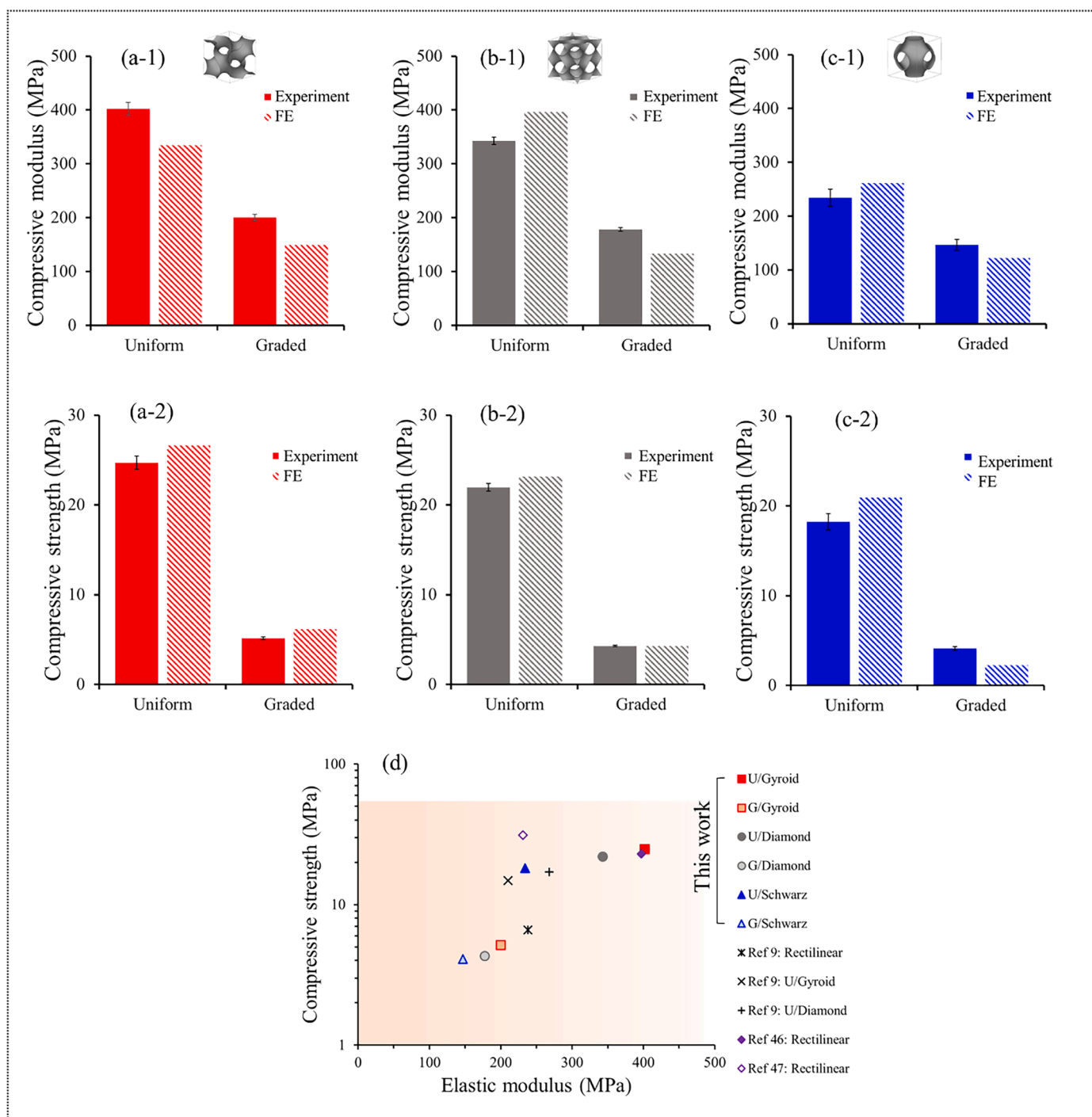


**Fig. 9.** Comparison of (1) Compressive modulus, and (2) Compressive strength for (a) Gyroid, (b) Diamond, and (c) Schwarz P scaffolds both uniform and graded structures, (d) Comparison of modulus and compressive strength between FDM-printed TPMS PEEK scaffolds in this study and existing literature on FDM-printed PEEK scaffolds. The obtained data shows close agreement with values reported for trabecular bone. The area filled with light red color highlights the range of mechanical properties typically observed in bone tissue.

The observed differences in compressive modulus and strength between the uniform and graded TPMS scaffolds can be attributed to various scientific factors. Firstly, the uniform scaffolds demonstrate higher compressive modulus and strength due to their more homogeneous and regular lattice configurations [53]. The uniform gyroid structure exhibits superior mechanical properties because of its inherent symmetry and interconnected network of struts [40]. This regularity allows for efficient load transfer and distribution, resulting in enhanced stiffness and strength. On the other hand, the graded scaffolds feature

variations in strut thickness, which introduce structural heterogeneity. These thickness variations affect the load-bearing capacity of the scaffold, leading to a reduction in compressive modulus and strength [47]. The thinner regions at the top surface of the graded structures are particularly susceptible to deformation and failure, contributing to the lower mechanical properties observed. While 3D scaffolds are designed to offer the necessary mechanical properties for compatibility at the implantation site, it's crucial that their geometry and architecture accurately replicates the natural structure of the host bones to facilitate

**Table 3**  
Compressive modulus and strength of FDM printed PEEK TPMS scaffolds obtained from experimental results and FE simulation.

	Compressive modulus E (MPa)		Compressive strength $\sigma$ (MPa)	
	Experimental	FE simulation	Experimental	FE simulation
Gyroid/ U	402	334	24.7	26.64
Gyroid/ G	200	149	5.15	6.15
Diamond/ U	343	396	21.96	23.16
Diamond/ G	178	133	4.3	4.3
Sch/ U	234	261	18.24	20.9
Sch/ G	147	122	4.1	2.22

tissue integration. It's important to note that geometrical requirements may vary at different stages of tissue regeneration. Therefore, the proper structural design of the scaffolds is crucial for creating an optimal growth environment, ensuring effective flow and diffusion of nutrients, waste, and other biomolecules [11,54]. In this context, porous scaffolds with gradients of geometrical features have been recognized to offer several advantages over uniform structures in clinical applications for bone defect repair. Gradient scaffolds can better mimic the natural gradient of properties found in bone tissue, such as stiffness and porosity, leading to improved tissue integration and regeneration [55]. The gradual variation in scaffold properties promotes cell migration, proliferation, and differentiation, facilitating tissue ingrowth and regeneration across the defect site. Additionally, gradient scaffolds allow for the customization of properties to match specific tissue

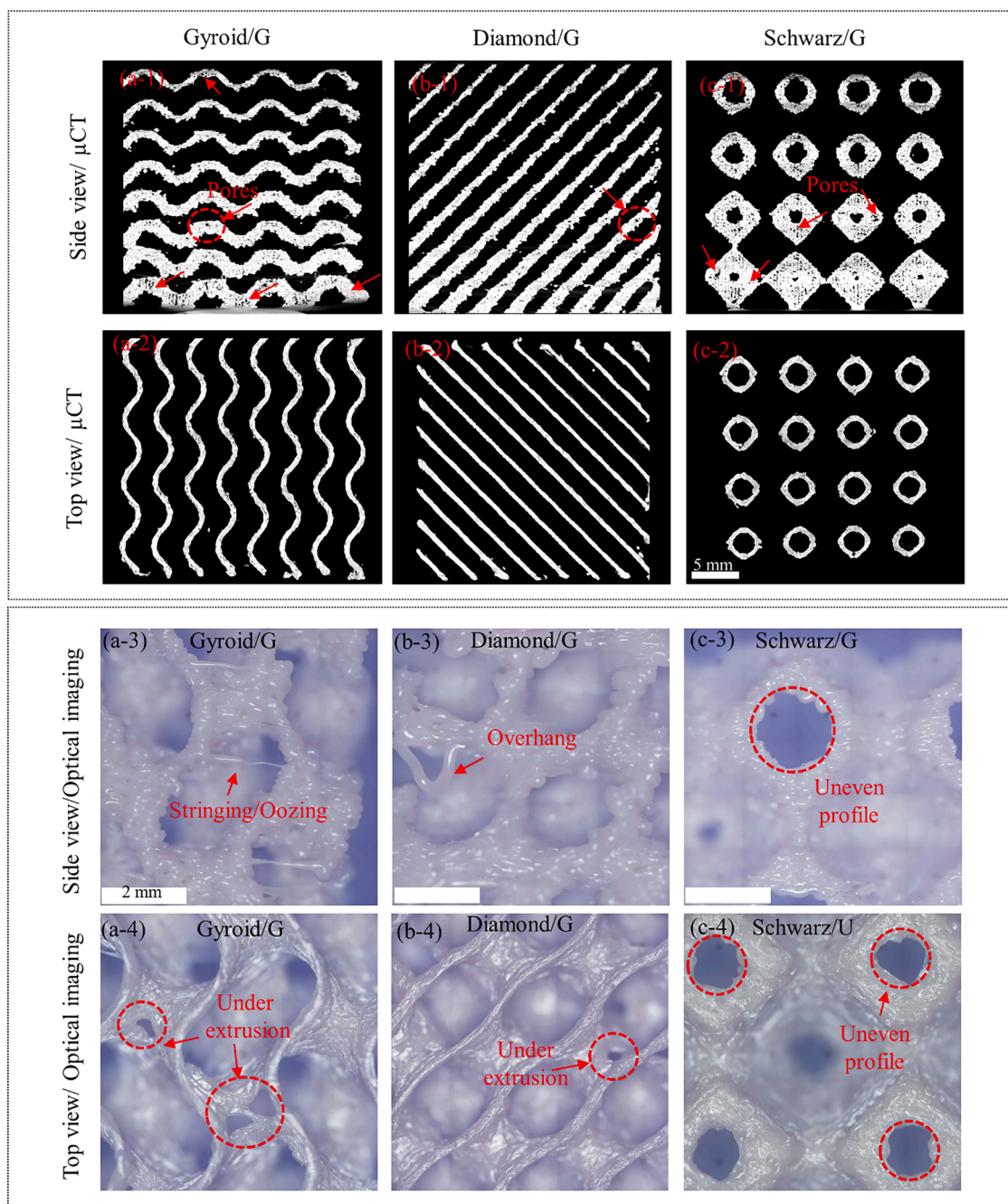


**Fig. 10.** 2D  $\mu$ CT rendering and Optical images revealing FDM process limitations in the fabrication of highly complex TPMS structures.  $\mu$ CT images from the top view were obtained from the XY plane 01 for all three graded scaffolds, showing the first top layer. U and G represent uniform and graded scaffolds, respectively.

requirements, enabling tailored treatments for individual patients and diverse defect geometries. By closely matching the mechanical properties of surrounding bone tissue, gradient scaffolds can reduce stress shielding effects, minimizing the risk of implant failure and promoting long-term stability [56]. The graded PEEK scaffold designed and FDM printed in this study has been conclusively proven to exhibit mechanical properties akin to trabecular bone while featuring a gradient structure. This innovative approach ensures the essential strength required while faithfully mirroring the hierarchical structure of bone.

### 3.4. Process limitation

TPMS surfaces with complex designs and curved contours are challenging geometries for FDM 3D printing process due to the steep overhangs and thin walls in the design. Nevertheless, the structures could be successfully fabricated, if the process parameters optimized well albeit with some structural errors [57]. Our study findings underscore some key limitations linked to FDM-printed TPMS PEEK scaffolds. These include the presence of voids and gaps between the extruded layers, as well as issues like stair-stepping effects, rippled surfaces and stringing. Additionally, the inherent self-supporting nature of TPMS structures may further contribute to inconsistencies in FDM-printed porous structures. It is worth noting that parts printed using the extrusion 3D printing technique exhibit anisotropic characteristics due to varying degrees of polymer chain interdiffusion and re-entanglement along both in-plane and out-of-plane directions. This anisotropic behavior can often result in layer delamination, potentially leading to brittle fracture properties. To mitigate this anisotropy, optimization of printing parameters such as the temperature of the nozzle, bed, and chamber, as well as nozzle geometries, use of additives and solvent, and post-processing techniques, is essential [58]. In our study, we relied on manufacturer recommendations for these printing parameters to ensure optimal fabrication conditions.

Fig. 10a-1, b-1, and c-1 provide 2D micro-CT renderings of graded Gyroid, Diamond, and Schwarz P scaffolds, showcasing the presence of small voids and tiny holes within the extruded layers. These observations align with the well-known issue of internal void formation during the FDM printing process, resulting from the layer-to-layer manufacturing approach and incomplete material filling within the part layers [59]. Furthermore, the micro-CT renderings from the top plane (Fig. 10a-2, b-2, and c-2) demonstrate a significant decrease in the number of voids observed on the scaffolds' upper surfaces. Additionally, the size of the voids appears to be smaller. Although meticulous optimization of the FDM process can substantially reduce the occurrence and size of voids and defects, it is advisable to employ post-processing techniques, such as chemical and heat treatments, to ensure complete filling of the voids [59].

Other limitations associated with the layer-by-layer nature of FDM printing are the presence of a stair-stepping effect, rippled surface appearance, and uneven profile shape which becomes more noticeable when viewing the FDM printed parts from the side. This effect is caused by the discrete deposition of material in each layer, leading to visible steps along the vertical axis [27,60]. However, the influence of material properties on these defects is significant. PEEK, known for its relatively high viscosity compared to other thermoplastics flows less easily due to its thicker consistency [61]. This reduced flowability results in more controlled material deposition during printing, minimizing the risk of over-extrusion. Consequently, high viscosity materials like PEEK are less prone to exhibiting rippled surface appearances caused by excessive material flow. Instead, they tend to produce smoother and more uniform surface finishes, showcasing the precision and reliability of their printing process.

Fig. 10c-3 and c-4 emphasize the issue of uneven profiles, which was particularly prominent in the case of Schwarz P structures. In addition to the aforementioned limitations, printing unsupported sections of TPMS curved surfaces and intricate details pose challenges, particularly in

regions with steep overhangs and sharp curves where there is no underlying layer for material adherence. The extrusion nozzle pulls and forms a straight segment of filament until it can attach to a stable surface, resulting in visible overhangs as illustrated in Fig. 10b-4. Furthermore, the stringing and oozing effect, caused by nozzle position changes, are more noticeable in these areas, as depicted in Fig. 10a-4.

Despite efforts to optimize printing parameters, such as controlled filament retraction, it is challenging to completely eliminate stringing effect, especially when printing complex contours. However, it is important to note that while stringing is generally considered a problem in FDM, it can have a significant positive impact in scaffolding applications by facilitating cell attachment [62]. Furthermore, Fig. 10a-4 and b-4 highlight the issue of the under-extrusion during the FDM printing process. Under-extrusion occurs when there is insufficient material deposited, leading to the formation of gaps or voids within the printed layers. This challenge becomes more pronounced in thin designs where the printer struggles to deposit the intended amount of material, leading to incomplete layer formation. Despite efforts to optimize printing parameters, such as using fine layer heights, improved nozzle geometries, and small diameters, and optimizing minimum infill length and print width, successfully FDM printing small features with steep overhanging regions and sharp curves remains a challenge. It is important to note that this effect was specifically observed in graded scaffolds with thin walls ranging from 450 to 700  $\mu\text{m}$  in thickness and a Z height of 25 mm. In contrast, under-extrusion was not observed in uniform scaffolds of all designs due to their larger strut thickness. Overall, despite some minor surface irregularities and inherent limitations of FDM printing, the scaffolds produced in this study demonstrated a high level of fidelity to the designed models with only minor deviations. Additionally, their mechanical properties were found to be in alignment with the requirements of cancellous bone. These findings underscore the potential of FDM printing as a viable and effective technique for fabricating complex and functional scaffolds for bone tissue engineering applications. By implementing postprocessing techniques such as heat and chemical treatments, it is possible to mitigate the limitations associated with FDM printing [63,64].

## 4. Conclusion

In this study and for the first time we have successfully utilized cost-effective FDM printing technology to fabricate density-graded PEEK TPMS scaffolds, including Gyroid, Diamond, and Schwarz P unit cell designs. The density-graded PEEK structures feature a continuous linear variation in wall thickness, ensuring a smooth relative density transition within the range of 22 % to 68 %, resulting in the same average porosity of 55 % as uniform scaffolds. Micro-CT and optical microscopy imaging confirm the accurate morphology of the FDM printed scaffolds compared to the CAD design models. Examination of the micro-CT and microscopy images reveals some minor structural and surface irregularities inherent to the layer-by-layer nature of the printing process. However, these imperfections did not significantly compromise the overall integrity and mechanical properties of the TPMS scaffolds. The Schwarz P scaffolds displayed larger pore sizes with more varied ranges compared to the Gyroid and Diamond scaffolds. The achievable pore sizes for graded Gyroid, Diamond, and Schwarz P scaffolds range from 590 to 1340  $\mu\text{m}$ , 700 to 1430  $\mu\text{m}$ , and 218 to 1745  $\mu\text{m}$ , respectively. Finite element simulation and compression tests were conducted to investigate the influence of unit cell design and gradient structure on stress distribution, deformation behavior, and mechanical properties. Findings revealed horizontal stress concentration in all density-graded structures with a higher concentration at the top surface, regardless of unit cell type. These top layers are typically the thinnest, making them more susceptible to deformation and collapse under compressive loading. This contrasted with lattice-dependent stress concentration observed in uniform structures. Notably, uniform Gyroid and Diamond scaffolds exhibited diagonal stress concentration, while Schwarz P

structure exhibited horizontal stress with concentration regions near the pore curves. Among the tested graded PEEK scaffolds, the Gyroid scaffold exhibited the highest elastic modulus and compressive strength, followed by the graded Diamond scaffold, while the graded Schwartz P scaffold show lower values. However, all gradient FDM printed PEEK TPMS scaffolds showcased elastic modulus and compressive strength closely resembling the properties of trabecular bone. In conclusion, this study has demonstrated that density-graded TPMS PEEK scaffolds with complex designs and curved contours can be fabricated using fast and cost-effective FDM printing technology to create diverse TPMS patterns, mirroring natural bone tissue in terms of continuous interconnectivity and mechanical characteristics. Among the three graded scaffold designs studied, the Gyroid and Diamond configurations stand out not only for displaying mechanical properties like trabecular bone and their ability to provide an ideal pore size range recommended for successful bone regeneration. However, future studies are needed to confirm the effectiveness of these designs utilizing PEEK material in promoting bone regeneration, both in vitro and in vivo.

### CRedit authorship contribution statement

**Nasim Sabahi:** Writing – original draft, Visualization, Validation, Software, Methodology, Investigation, Formal analysis, Data curation, Conceptualization. **Ehsan Farajzadeh:** Writing – review & editing, Visualization, Validation, Software, Formal analysis, Data curation. **Iman Roohani:** Writing – review & editing. **Chun H. Wang:** Writing – review & editing. **Xiaopeng Li:** Writing – review & editing, Supervision, Funding acquisition.

### Declaration of competing interest

The authors declare that they have no known competing financial interests or personal relationships that could have appeared to influence the work reported in this paper.

### Data availability

Data will be made available on request.

### Acknowledgements

N.S. expresses gratitude for the financial assistance received from UNSW, which includes support through a PhD research scholarship and postdoctoral writing fellowship. The authors are grateful for the scientific and technical support, as well as the facilities provided by the UNSW Tyree X-ray micro-CT facility.

### Supplementary materials

Supplementary material associated with this article can be found, in the online version, at [doi:10.1016/j.apmt.2024.102262](https://doi.org/10.1016/j.apmt.2024.102262).

### References

- Z. Du, Z. Zhu, B. Yue, Z. Li, Y. Wang, Feasibility and Safety of a cemented PEEK-on-PE knee replacement in a goat model: a preliminary study, *Artif. Organs* 42 (8) (2018) E204–E214, <https://doi.org/10.1111/aor.13101>.
- S.M. Kurtz, Chapter 13 - applications of Polyaryletheretherketone in spinal implants: fusion and motion preservation, in: S.M. Kurtz (Ed.), *PEEK Biomaterials Handbook*, Oxford: William Andrew Publishing, 2012, pp. 201–220, <https://doi.org/10.1016/B978-1-4377-4463-7.10013-2>.
- B.C. Landy, S.B. VanGordon, P.S. McFetridge, V.I. Sikavitsas, M. Jarman-Smith, Mechanical and in vitro investigation of a porous PEEK foam for medical device implants, *J. Appl. Biomater. Funct. Mater.* 11 (1) (2013) 35–44, <https://doi.org/10.5301/JABFM.2012.9771>.
- S.M. Kurtz, J.N. Devine, PEEK biomaterials in trauma, orthopedic, and spinal implants, *Biomaterials* 28 (32) (2007) 4845–4869, <https://doi.org/10.1016/j.biomaterials.2007.07.013>.
- S. Boriani, et al., Carbon-fiber-reinforced PEEK fixation system in the treatment of spine tumors: a preliminary report, *Eur. Spine J.* 27 (4) (2018) 874–881, <https://doi.org/10.1007/s00586-017-5258-5>.
- D.W. Huttmacher, Scaffold design and fabrication technologies for engineering tissues - State of the art and future perspectives, *J. Biomater. Sci. Polym. Ed.* 12 (1) (2001) 107–124, <https://doi.org/10.1163/156856201744489>.
- A.R. Amini, C.T. Laurencin, S.P. Nukavarapu, Bone tissue engineering: recent advances and challenges, *Crit. Rev. Biomed. Eng.* 40 (5) (2012) 363–408, <https://doi.org/10.1615/CritRevBiomedEng.v40.i5.10>.
- D.J. Yoo, Computer-aided porous scaffold design for tissue engineering using triply periodic minimal surfaces, *Int. J. Precis. Eng. Manuf.* 12 (1) (2011) 61–71, <https://doi.org/10.1007/s12541-011-0008-9>.
- S.B.G. Blanquer, et al., Surface curvature in triply-periodic minimal surface architectures as a distinct design parameter in preparing advanced tissue engineering scaffolds, *Biofabrication* 9 (2) (2017), <https://doi.org/10.1088/1758-5090/aa6553>.
- S. Vijayavenkataraman, L. Zhang, S. Zhang, J.Y.H. Fuh, W.F. Lu, Triply periodic minimal surfaces sheet scaffolds for tissue engineering applications: an optimization approach toward biomimetic scaffold design, *ACS Appl. Bio Mater* 1 (2) (2018) 259–269, <https://doi.org/10.1021/acsbam.8b00052>.
- F. Liu, Z. Mao, P. Zhang, D.Z. Zhang, J. Jiang, Z. Ma, Functionally graded porous scaffolds in multiple patterns: new design method, physical and mechanical properties, *Mater. Des.* 160 (2018) 849–860, <https://doi.org/10.1016/j.matdes.2018.09.053>.
- O. Al-Ketan, R. Rowshan, R.K. Abu Al-Rub, “Topology-mechanical property relationship of 3D printed strut, skeletal, and sheet based periodic metallic cellular materials, *Addit. Manuf.* 19 (2018) 167–183, <https://doi.org/10.1016/j.addma.2017.12.006>.
- C.N. Kelly, et al., Fatigue behavior of As-built selective laser melted titanium scaffolds with sheet-based gyroid microarchitecture for bone tissue engineering, *Acta Biomater* 94 (2019) 610–626, <https://doi.org/10.1016/j.actbio.2019.05.046>.
- B. Liao, R.F. Xia, W. Li, D. Lu, Z.M. Jin, 3D-Printed Ti6Al4V scaffolds with graded triply periodic minimal surface structure for bone tissue engineering, *J. Mater. Eng. Perform.* 30 (7) (2021) 4993–5004, <https://doi.org/10.1007/s11665-021-05580-z>.
- L. Yang, C. Yan, C. Han, P. Chen, S. Yang, Y. Shi, Mechanical response of a triply periodic minimal surface cellular structures manufactured by selective laser melting, *Int. J. Mech. Sci.* 148 (2018) 149–157, <https://doi.org/10.1016/j.ijmecsci.2018.08.039>. August.
- N. Sabahi, W. Chen, C.H. Wang, J.J. Kruzic, X. Li, A review on additive manufacturing of shape-memory materials for biomedical applications, *JOM* 72 (3) (2020) 1229–1253, <https://doi.org/10.1007/s11837-020-04013-x>.
- H. Wang, et al., Comparative evaluation of printability and compression properties of poly-ether-ether-ketone triply periodic minimal surface scaffolds fabricated by laser powder bed fusion, *Addit. Manuf.* 57 (2022), <https://doi.org/10.1016/j.addma.2022.102961>.
- P. Chen, et al., Mechanical properties and microstructure characteristics of lattice-surfaced PEEK cage fabricated by high-temperature laser powder bed fusion, *J. Mater. Sci. Technol.* 125 (2022) 105–117, <https://doi.org/10.1016/j.jmst.2022.03.009>.
- M. Salmi, Additive manufacturing processes in medical applications, *Materials (Basel)* 14 (1) (2021) 1–16, <https://doi.org/10.3390/ma14010191>.
- W. Jamroz, J. Szafraniec, M. Kurek, R. Jachowicz, 3D printing in pharmaceutical and medical applications – recent achievements and challenges, *Pharm. Res.* 35 (9) (2018), <https://doi.org/10.1007/s11095-018-2454-x>.
- P. Chen, et al., Recent advances on high-performance polyaryletherketone materials for additive manufacturing, *Adv. Mater.* 34 (52) (2022) 1–26, <https://doi.org/10.1002/adma.202200750>.
- K. Elhattab, P. Sikder, J.M. Walker, M.C. Bottino, S.B. Bhaduri, Fabrication and evaluation of 3-D printed PEEK scaffolds containing macropores by design, *Mater. Lett.* 263 (2020) 3–6, <https://doi.org/10.1016/j.matlet.2019.127227>.
- Y. Su, et al., Additively-manufactured poly-ether-ether-ketone (PEEK) lattice scaffolds with uniform microporous architectures for enhanced cellular response and soft tissue adhesion, *Mater. Des.* 191 (2020) 108671, <https://doi.org/10.1016/j.matdes.2020.108671>.
- X. Feng, et al., Osteointegration of 3D-printed fully porous polyetheretherketone scaffolds with different pore sizes, *ACS Omega* 5 (41) (2020) 26655–26666, <https://doi.org/10.1021/acsomega.0c03489>.
- B.I. Oladapo, S.O. Ismail, O.K. Bowoto, F.T. Omigbodun, M.A. Olowumi, M. A. Muhammad, Lattice design and 3D-printing of PEEK with Ca10(OH)(PO4)3 and in-vitro bio-composite for bone implant, *Int. J. Biol. Macromol.* 165 (2020) 50–62, <https://doi.org/10.1016/j.ijbiomac.2020.09.175>.
- H. Spece, T. Yu, A.W. Law, M. Marcolongo, S.M. Kurtz, 3D printed porous PEEK created via fused filament fabrication for osteoconductive orthopaedic surfaces, *J. Mech. Behav. Biomed. Mater.* 109 (2020), <https://doi.org/10.1016/j.jmbm.2020.103850>.
- H. Spece, P.M. DeSantis, S.M. Kurtz, Development of an architecture-property model for triply periodic minimal surface structures and validation using material extrusion additive manufacturing with polyetheretherketone (PEEK), *J. Mech. Behav. Biomed. Mater.* 133 (2022), <https://doi.org/10.1016/j.jmbm.2022.105345>. January.
- Y. Liu, D. Luo, T. Wang, Hierarchical structures of bone and bioinspired bone tissue engineering, *Small* 12 (34) (2016) 4611–4632, <https://doi.org/10.1002/sml.201600626>.
- C. Erskens, D.M. Kalyon, H. Wang, Functionally graded electrospun polycaprolactone and  $\beta$ -tricalcium phosphate nanocomposites for tissue

- engineering applications, *Biomaterials* 29 (30) (2008) 4065–4073, <https://doi.org/10.1016/j.biomaterials.2008.06.022>.
- [30] M.N. Collins, G. Ren, K. Young, S. Pina, R.L. Reis, J.M. Oliveira, Scaffold fabrication technologies and structure/function properties in bone tissue engineering, *Adv. Funct. Mater.* 31 (21) (2021), <https://doi.org/10.1002/adfm.202010609>. John Wiley and Sons Inc.
- [31] S.J. Seo, C. Mahapatra, R.K. Singh, J.C. Knowles, H.W. Kim, Strategies for osteochondral repair: focus on scaffolds, *J. Tissue Eng.* 5 (2014), <https://doi.org/10.1177/2041731414541850>. SAGE Publications Ltd.
- [32] C. Han, et al., Continuous functionally graded porous titanium scaffolds manufactured by selective laser melting for bone implants, *J. Mech. Behav. Biomed. Mater.* 80 (2018) 119–127, <https://doi.org/10.1016/j.jmbbm.2018.01.013>.
- [33] F.P.W. Melchels, K. Bertoldi, R. Gabrielli, A.H. Velders, J. Feijen, D.W. Grijpma, Mathematically defined tissue engineering scaffold architectures prepared by stereolithography, *Biomaterials* 31 (27) (2010) 6909–6916, <https://doi.org/10.1016/j.biomaterials.2010.05.068>.
- [34] D.J. Yoo, Porous scaffold design using the distance field and triply periodic minimal surface models, *Biomaterials* 32 (31) (2011) 7741–7754, <https://doi.org/10.1016/j.biomaterials.2011.07.019>.
- [35] C.M. Murphy, M.G. Haugh, F.J. O'Brien, The effect of mean pore size on cell attachment, proliferation and migration in collagen-glycosaminoglycan scaffolds for bone tissue engineering, *Biomaterials* 31 (3) (2010) 461–466, <https://doi.org/10.1016/j.biomaterials.2009.09.063>.
- [36] N. Yang, Y. Tian, D. Zhang, Novel real function based method to construct heterogeneous porous scaffolds and additive manufacturing for use in medical engineering, *Med. Eng. Phys.* 37 (11) (2015) 1037–1046, <https://doi.org/10.1016/j.medengphy.2015.08.006>.
- [37] D. Carluccio, et al., Additively manufactured iron-manganese for biodegradable porous load-bearing bone scaffold applications, *Acta Biomater.* 103 (2020) 346–360, <https://doi.org/10.1016/j.actbio.2019.12.018>.
- [38] C. Basgul, D.W. MacDonald, R. Siskey, S.M. Kurtz, Thermal localization improves the interlayer adhesion and structural integrity of 3D printed PEEK lumbar spinal cages, *Materialia* 10 (2020), <https://doi.org/10.1016/j.mtla.2020.100650>. January.
- [39] A. Standard, *Standard Test Method For Compressive Properties of Rigid Plastics*, 2015.
- [40] I. Maskery, N.T. Aboulkhair, A.O. Aremu, C.J. Tuck, I.A. Ashcroft, Compressive failure modes and energy absorption in additively manufactured double gyroid lattices, *Addit. Manuf.* 16 (2017) 24–29, <https://doi.org/10.1016/j.addma.2017.04.003>.
- [41] U.M. Dilberoglu, S. Simsek, U. Yaman, Shrinkage compensation approach proposed for ABS material in FDM process, *Mater. Manuf. Process.* 34 (9) (2019) 993–998, <https://doi.org/10.1080/10426914.2019.1594252>.
- [42] I. Bute, S. Tarasovs, S. Vidinejevs, L. Vevere, J. Sevckenko, A. Aniskevich, Thermal properties of 3D printed products from the most common polymers, *Int. J. Adv. Manuf. Technol.* 124 (7–8) (2023) 2739–2753, <https://doi.org/10.1007/s00170-022-10657-7>.
- [43] L. Karthikeyan, et al., Poly(ether ether ketone)s processed through extrusion-machining and 3D printing: a comparative study on mechanical, thermal and fracture properties at ambient and cryogenic environments, *J. Elastomers Plast.* 53 (6) (2021) 672–683, <https://doi.org/10.1177/0095244320961830>.
- [44] B. Otsuki, M. Takemoto, S. Fujibayashi, M. Neo, T. Kokubo, T. Nakamura, Pore throat size and connectivity determine bone and tissue ingrowth into porous implants: three-dimensional micro-CT based structural analyses of porous bioactive titanium implants, *Biomaterials* 27 (35) (2006) 5892–5900, <https://doi.org/10.1016/j.biomaterials.2006.08.013>.
- [45] F. Shi, et al., Macropore regulation of hydroxyapatite osteoinduction via microfluidic pathway, *Int. J. Mol. Sci.* 23 (19) (2022), <https://doi.org/10.3390/ijms231911459>.
- [46] F. Lu, et al., Journal of the European ceramic society rational design of bioceramic scaffolds with tuning pore geometry by stereolithography : microstructure evaluation and mechanical evolution, *J. Eur. Ceram. Soc.* 41 (2) (2021) 1672–1682, <https://doi.org/10.1016/j.jeurceramsoc.2020.10.002>.
- [47] S. Yu, J. Sun, J. Bai, Investigation of functionally graded TPMS structures fabricated by additive manufacturing, *Mater. Des.* 182 (2019), <https://doi.org/10.1016/j.matdes.2019.108021>.
- [48] A. Rege, Constitutive modeling of the densification behavior in open-porous cellular solids, *Materials (Basel)* 14 (11) (2021) 1–10, <https://doi.org/10.3390/ma14112731>.
- [49] L. Zhang, et al., Energy absorption characteristics of metallic triply periodic minimal surface sheet structures under compressive loading, *Addit. Manuf.* 23 (2018) 505–515, <https://doi.org/10.1016/j.addma.2018.08.007>.
- [50] J. Feng, J. Fu, X. Yao, Y. He, Triply periodic minimal surface (TPMS) porous structures: from multi-scale design, precise additive manufacturing to multidisciplinary applications, *Int. J. Extrem. Manuf.* 4 (2) (2022), <https://doi.org/10.1088/2631-7990/ac5be6>.
- [51] E.F. Morgan, T.M. Keaveny, Dependence of yield strain of human trabecular bone on anatomic site, *J. Biomech.* 34 (5) (2001) 569–577, [https://doi.org/10.1016/S0021-9290\(01\)00011-2](https://doi.org/10.1016/S0021-9290(01)00011-2).
- [52] E.F. Morgan, G.U. Unnikrisnan, A.I. Hussein, *Bone Mechanical Properties in Healthy and Diseased States*, 2018.
- [53] F. Liu, Z. Mao, P. Zhang, D.Z. Zhang, J. Jiang, Z. Ma, Functionally graded porous structures in multiple patterns: new design method, physical and mechanical properties, *Mater. Des.* 160 (2018), <https://doi.org/10.1016/j.matdes.2018.09.053>.
- [54] A.A. Zadpoor, Bone tissue regeneration: the role of scaffold geometry, *Biomater. Sci.* 3 (2) (2015) 231–245, <https://doi.org/10.1039/c4bm00291a>.
- [55] N. Yang, K. Zhou, Effective method for multi-scale gradient porous scaffold design and fabrication, *Mater. Sci. Eng. C* 43 (2014) 502–505, <https://doi.org/10.1016/j.msec.2014.07.052>.
- [56] M.A. Surmeneva, et al., Fabrication of multiple-layered gradient cellular metal scaffold via electron beam melting for segmental bone reconstruction, *Mater. Des.* 133 (2017) 195–204, <https://doi.org/10.1016/j.matdes.2017.07.059>.
- [57] C. Kenel, J.P.W. Sesseg, N.R. Geisendorfer, R.N. Shah, R. Spolenak, D.C. Dunand, 3D-printed tungsten sheet-gyroids via reduction and sintering of extruded WO<sub>3</sub>-nanopowder inks, *Addit. Manuf.* 36 (2020), <https://doi.org/10.1016/j.addma.2020.101613>.
- [58] J. Chen, et al., 3D-printed anisotropic polymer materials for functional applications, *Adv. Mater.* 34 (5) (2022) 1–33, <https://doi.org/10.1002/adma.202102877>.
- [59] X. Sun, M. Mazur, C.T. Cheng, A review of void reduction strategies in material extrusion-based additive manufacturing, *Addit. Manuf.* 67 (2023) 103463, <https://doi.org/10.1016/j.addma.2023.103463>. February.
- [60] L. Yang, et al., An investigation into the effect of gradients on the manufacturing fidelity of triply periodic minimal surface structures with graded density fabricated by selective laser melting, *J. Mater. Process. Technol.* 275 (2020) 116367, <https://doi.org/10.1016/j.jmatprotec.2019.116367>. February 2019.
- [61] P. Wang, B. Zou, H. Xiao, S. Ding, C. Huang, Effects of printing parameters of fused deposition modeling on mechanical properties, surface quality, and microstructure of PEEK, *J. Mater. Process. Technol.* 271 (2019) 62–74, <https://doi.org/10.1016/j.jmatprotec.2019.03.016>. February.
- [62] S. Gnanamani Sankaravel, R.B. Syed, V. Manivachakan, In vitro and mechanical characterization of PLA/egg shell biocomposite scaffold manufactured using fused deposition modeling technology for tissue engineering applications, *Polym. Compos.* 43 (1) (2022) 173–186, <https://doi.org/10.1002/pc.26365>.
- [63] N. Jayanth, P. Senthil, C. Prakash, Effect of chemical treatment on tensile strength and surface roughness of 3D-printed ABS using the FDM process, *Virtual Phys. Prototyp.* 13 (3) (2018) 155–163, <https://doi.org/10.1080/17452759.2018.1449565>.
- [64] A. Garg, A. Bhattacharya, A. Batish, Effect of cold vapour treatment on geometric accuracy of fused deposition modelling parts, *Rapid Prototyp. J.* 23 (6) (2017) 1226–1236, <https://doi.org/10.1108/RPJ-05-2016-0072>.